

# Antiferromagnetic magnons and local anisotropy: dynamical mean-field study

A. Niyazi,<sup>1</sup> D. Geffroy,<sup>2,1</sup> and J. Kuneš<sup>1</sup>

<sup>1</sup>*Institute of Solid State Physics, TU Wien, 1040 Vienna, Austria*

<sup>2</sup>*Department of Condensed Matter Physics, Faculty of Science,  
Masaryk University, Kotlářská 2, 611 37 Brno, Czechia*

(Dated: September 10, 2021)

We present a dynamical mean-field study of antiferromagnetic magnons in one-, two- and three-orbital Hubbard model of square and bcc cubic lattice at intermediate coupling strength. We investigate the effect of anisotropy introduced by an external magnetic field or single-ion anisotropy. For the latter we tune continuously between the easy-axis and easy-plane models. We also analyze a model with spin-orbit coupling in cubic site-symmetry setting. The ordered states as well as the magnetic excitations are sensitive to even a small breaking of  $SU(2)$  symmetry of the model and follow the expectations of spin-wave theory as well as general symmetry considerations.

## I. INTRODUCTION

The scalability to multi-orbital systems made the dynamical mean-field theory (DMFT) [1–3] a widely used tool for the investigation of electronic correlations on material specific level [4, 5]. The primary niche of DMFT are the one-particle correlation functions (1PCFs) such as the generalized band structures. Nevertheless, DMFT allows the calculation of higher order correlation functions as well. In particular, two-particle correlation functions (2PCFs) play a crucial role in the description of continuous phase transitions and, in the form of transport coefficients, dynamical structure factors or susceptibilities are directly related to numerous experiments. The solution of the Bethe-Salpeter equation (BSE) makes the calculation of 2PCFs numerically very demanding. The DMFT calculations of 2PCFs have so far been limited to simple models and high symmetry [6–10], or have involved substantial approximations [11]. Numerical and analytical developments in representation of 2PCFs [12] and solution of BSE [13–16] make calculations for realistic models with three or more orbitals and several atoms in the unit cell feasible.

The collective modes described by 2PCFs play a particularly important role in ordered phases with spontaneously broken symmetry. Presence or absence of a gap in 2PCF spectrum related to the type, discrete vs continuous, of broken symmetry is decisive for finite-temperature stability of the ordered state in two dimensions [17]. Therefore it is important to understand not only the analytic properties of a given theory, for DMFT see Refs. 18–20, but also the properties of the actual numerical implementation. Recently, some of us demonstrated [21, 22] that the dynamical susceptibilities obtained using DMFT respect the Goldstone theorem [23, 24] in the case of  $U(1) \times U(1)$  symmetry breaking in spinful excitonic condensate [25–27].

The most common and largely studied long-range order in strongly correlated materials is the antiferromagnetic (AFM) one [28]. The AFM Heisenberg model [29], which describes fluctuating spins in Mott insulators, was studied in detail with analytical [30] as well as with numerically

exact methods [31]. Investigation of antiferromagnetism in the fermionic Hubbard model, which allows for the description of doped Mott insulators or AFM metals, relies on weak-coupling methods such as the random phase approximation [32, 33], two-particle self-consistent approximation [34] or fluctuation-exchange approximation [35], numerical simulations on finite systems [36, 37] or local approximations to interaction vertices such as DMFT and its cluster [38, 39] or diagrammatic extensions [40, 41].

In this Article, we use DMFT and 2PCFs to study AFM ordering in the half-filled Hubbard model with one, two and three orbitals. While the magnetic phase diagram of the single-orbital Hubbard model in three dimensions (3D) has been investigated with a number of methods [38, 39, 42] including DMFT [38, 42, 43], we calculate the magnon spectra and we introduce various symmetry breaking terms such as external field or single-ion anisotropy, in order to analyze their effect on magnon dispersions. The calculations are performed for 2D and 3D lattices. Our goal is to demonstrate the utility of the present approach for the study of the magnetically ordered phases of multi-orbital models. In the 2D case, where spontaneous symmetry breaking is forbidden in the case of continuous symmetry [17] but allowed in case of discrete symmetry, we investigate a model, which can be continuously tuned between these cases.

## II. COMPUTATIONAL METHOD

The studied Hamiltonian consists of the inter-site hopping, diagonal in orbital and spin indices, and the on-site part  $H_i$  consisting of the electron-electron interaction, external Zeeman field and spin-orbit coupling (the specific form will be given later for each studied case)

$$H = t \sum_{\langle ij \rangle, \sigma} \sum_{l=1}^N c_{il\sigma}^\dagger c_{jl\sigma} + \sum_i H_i. \quad (1)$$

Here,  $c_{il\sigma}^\dagger$  and  $c_{il\sigma}$  are the fermionic creation and annihilation operators for electrons with spin  $\sigma$  in orbital

$l$  at site  $i$  of a square or bcc cubic lattice. The number of orbitals  $N$  ranges from 1 to 3 in the studied models. For later use we define the occupation number operator  $n_{i\sigma} \equiv c_{i\sigma}^\dagger c_{i\sigma}$  and the local spin operators  $S_i^\alpha \equiv \sum_{\nu\nu'} \sigma_{\nu\nu'}^\alpha c_{i\nu}^\dagger c_{i\nu'}$ , where  $\sigma^\alpha$  are the Pauli matrices. For the sake of consistency with previous work [44] we choose  $t = 1/8$  and use it for all studied cases.

The calculations follow the standard DMFT procedure. The lattice model is mapped onto an auxiliary Anderson impurity model with self-consistently determined parameters [2, 6], for which the 1PCFs are evaluated using the ALPS implementation [45–47] of the strong-coupling continuous-time quantum Monte-Carlo (CT-QMC) algorithm [48]. The model hosts two competing phases: the normal paramagnetic one and the AFM phase with a staggered spin configuration characterized by the Néel vector  $\mathbf{N} = \frac{1}{2}(\mathbf{S}_A - \mathbf{S}_B)$ . We focus on the dynamical spin susceptibility  $\chi^{\alpha\alpha}(\mathbf{q}, \omega)$ , which is obtained by analytic continuation from its Matsubara representation

$$\frac{1}{N} \langle \tilde{S}_{-\mathbf{q}}^\alpha \tilde{S}_{\mathbf{q}}^\alpha \rangle_{\omega_n} = \frac{1}{N} \int_0^\beta d\tau e^{i\omega_n \tau} \langle \tilde{S}_{-\mathbf{q}}^\alpha(\tau) \tilde{S}_{\mathbf{q}}^\alpha(0) \rangle. \quad (2)$$

Here  $\langle X \rangle = \frac{1}{Z} \text{Tr} X e^{-\beta H}$  denotes the thermal average,  $N$  is the number of lattice sites and  $\tilde{X} = X - \langle X \rangle$ . We also evaluate the 1P observables such as the static magnetization  $\langle \mathbf{S}_{\mathbf{R}} \rangle$  and the 1P spectral functions. The analytic continuation employs the maximum entropy method [49], for details of the present implementation see Refs. 21 and 50.

The calculations are performed in a two-site unit cell where the sites are labeled by the sublattice index  $s = A, B$ . The reciprocal space operators in Eq. 2 are then given by  $\tilde{S}_{\mathbf{q}}^\alpha = \sum_{\mathbf{R}} e^{-i\mathbf{q} \cdot \mathbf{R}} \left( \tilde{S}_{\mathbf{R},A}^\alpha + e^{-i\mathbf{q} \cdot \mathbf{s}} \tilde{S}_{\mathbf{R},B}^\alpha \right)$ , where the sublattice vector  $\mathbf{s}$  assumes the value  $(\frac{1}{2}, \frac{1}{2})$  or  $(\frac{1}{2}, \frac{1}{2}, \frac{1}{2})$  for the 2D and 3D models, respectively. The

correlation function in Eq. 2 is then obtained as a linear combination of the sublattice contributions

$$\begin{aligned} \langle \tilde{S}_{-\mathbf{q}} \tilde{S}_{\mathbf{q}} \rangle_{\omega} &= \langle \tilde{S}_{-\mathbf{q},A} \tilde{S}_{\mathbf{q},A} \rangle_{\omega} + \langle \tilde{S}_{\mathbf{q},B} \tilde{S}_{-\mathbf{q},B} \rangle_{\omega} \\ &+ e^{i\mathbf{q} \cdot \mathbf{s}} \langle \tilde{S}_{-\mathbf{q},B} \tilde{S}_{\mathbf{q},A} \rangle_{\omega} + e^{-i\mathbf{q} \cdot \mathbf{s}} \langle \tilde{S}_{-\mathbf{q},A} \tilde{S}_{\mathbf{q},B} \rangle_{\omega}. \end{aligned}$$

Each term is a contraction of the generalized susceptibility  $\chi_{ijs,kl s'}(\mathbf{q}, \omega)$  over the spin-orbital indices

$$\frac{1}{N} \langle \tilde{S}_{-\mathbf{q},s}^\alpha \tilde{S}_{\mathbf{q},s'}^\alpha \rangle_{\omega} = M_{ij}^\alpha M_{kl}^\alpha \chi_{ijs,kl s'}(\mathbf{q}, \omega).$$

with matrix elements  $M_{ij}^\alpha$  following from the definition of the spin operators above. To simplify the notation we use underline to indicate summation over the corresponding indices [51].

The calculation of the generalized susceptibility within DMFT [3, 6, 7, 44] requires a more general object – the 2PCF  $X_{ijs\nu,kl s'\nu'}(\mathbf{q}, \omega)$ , where  $i, j, k, l$  are the spin-orbital indices,  $s, s'$  are the sublattice indices, and  $\nu, \nu'$  are fermionic indices, which represent the imaginary time evolution, e.g. Matsubara frequencies or imaginary time. Since the fermionic indices appear only as dummy variables in the BSE, the equation is invariant under their unitary transformation. In the present calculations we use the Legendre basis [7] for the fermionic indices. The susceptibility  $\chi_{\dots\dots\dots}(\mathbf{q}, \omega)$  is obtained by the contraction of  $X_{\dots\nu\dots\nu'}(\mathbf{q}, \omega)$  with the basis dependent structure factor  $F_\nu$  [7] [52]

$$\chi_{ijs,kl s'}(\mathbf{q}, \omega) = F_\nu F_{\nu'} X_{ijs\nu,kl s'\nu'}(\mathbf{q}, \omega). \quad (3)$$

The 2PCF  $X_{ijs\nu,kl s'\nu'}(\mathbf{q}, \omega)$  is the solution of the lattice BSE (4) using the local 2P-irreducible vertices  $\Gamma_{ij\nu,kl\nu'}^s(\omega)$  and the lattice bubbles  $X_{ijs\nu,kl s'\nu'}^0(\mathbf{q}, \omega)$ . The vertices are related to the impurity 2PCF  $x_{ij\nu,kl\nu'}(s; \omega)$  via the impurity BSE (5) for each sublattice  $s$ .

$$X_{ijs\nu,kl s'\nu'}(\mathbf{q}, \omega) = X_{ijs\nu,kl s'\nu'}^0(\mathbf{q}, \omega) + X_{ijs\nu,mn s_1\nu_1}^0(\mathbf{q}, \omega) \Gamma_{mn\nu_1,pq\nu_2}^{s_1}(\omega) X_{pq s_1\nu_2,kl s'\nu'}(\mathbf{q}, \omega) \quad (4)$$

$$x_{ij\nu,kl\nu'}(s; \omega) = x_{ij\nu,kl\nu'}^0(s; \omega) + x_{ij\nu,mn\nu_1}^0(s; \omega) \Gamma_{mn\nu_1,pq\nu_2}^s(\omega) x_{pq\nu_2,kl\nu'}(s; \omega). \quad (5)$$

The lattice and local bubbles

$$\begin{aligned} X_{ijs\nu,kl s'\nu'}^0(\mathbf{q}, \omega) &= -\delta_{\nu\nu'} G_{is,ks'}(\underline{\mathbf{k}} + \mathbf{q}, \nu + \omega) G_{ls',js}(\underline{\mathbf{k}}, \nu) \\ x_{ij\nu,kl\nu'}^0(s; \omega) &= -\delta_{\nu\nu'} G_{is,ks}(\underline{\mathbf{k}}, \nu + \omega) G_{ls,js}(\underline{\mathbf{k}}', \nu). \end{aligned}$$

are obtained from the 1P propagator

$$G_{is,js'}(\mathbf{k}, \nu) = [i\nu - h_{\mathbf{k}} - \Sigma(\nu)]_{is,js'}^{-1}.$$

Note that in the 2P quantities, such as  $X_{ijs\nu,kl s'\nu'}(\mathbf{q}, \omega)$ , the spin-orbital indices  $i$  and  $j$  ( $k$  and  $l$ ) point to the

same lattice site and thus share the sublattice index  $s$  ( $s'$ ). This is because we are interested in correlators of local operators, i.e., products of the type  $c_{\mathbf{R}s\dots}^\dagger c_{\mathbf{R}s\dots}$ , and because the DMFT vertex  $\Gamma_{jk\nu,kl\nu'}^s(\omega)$  is local. As a result the corresponding matrices scale with the square of the number of spin-orbitals per site  $2N$ , but only linearly with the number of sites per unit cell.

We used the 1P propagators at 300 Matsubara frequencies and a uniform  $55 \times 55$  ( $25 \times 25 \times 25$ )  $k$ -mesh in the 2D (3D) case to compute the lattice and local

bubbles  $X_{ijs\nu,kl\nu'}(\mathbf{q},\omega)$  and  $x_{ij\nu,kl\nu'}^0(s;\omega)$ . These are then transformed into the Legendre representation [7]. The 2P correlation function  $x_{ij\nu,kl\nu'}(s;\omega)$  is sampled using the CT-QMC directly in the Legendre basis. The local 2P-irreducible vertex  $\Gamma_{ij\nu,kl\nu'}^s(\omega)$  is obtained from the impurity BSE (5). Next we solve the lattice BSE (4) independently for each bosonic Matsubara frequency and  $\mathbf{q}$ -point. We use from 22 (for the zeroth bosonic frequency) to 45 Legendre coefficients (for the fourteenth bosonic frequency). A sizable reduction of the computational and storage cost can be achieved with the procedure of Refs. 12 and 53.

We found that 15 bosonic Matsubara frequencies allow for a stable analytic continuation in the low-energy region, which for the chosen interaction strengths dominates over the high-energy particle-hole continuum, which we do not attempt to extract. In particular, it allows to detect the opening of spin gaps and the suppression of otherwise divergent spectral weights caused by minor lowering of the Hamiltonian symmetry. Given the insufficient data statistics we have used a conservative estimate of the uncorrelated standard deviations of 0.02 at each Matsubara frequency point [50]. Similar calculations for weaker interaction strength, for which the particle-hole continuum co-exists with magnon modes, would require more Matsubara frequencies.

The spectral functions  $B_{\mathbf{k}}^{\alpha\alpha}(\omega) = -\frac{1}{\pi} \text{Im} \chi^{\alpha\alpha}(\mathbf{q},\omega)$  are our final product. Given the divergence of  $B_{\mathbf{k}}(\omega)$  at the ordering wave vector, we introduce an effective cutoff by plotting  $\tilde{B}_{\mathbf{k}}(\omega) = \frac{B_{\mathbf{k}}(\omega)}{C+B_{\mathbf{k}}(\omega)}$  instead of  $B_{\mathbf{k}}(\omega)$  itself. To represent the amplitude we also plot the spectral weight  $\Omega_{\mathbf{k}} = \int_0^{0.5} B_{\mathbf{k}}(\omega)d\omega$ .

### III. RESULTS AND DISCUSSION

#### A. S=1/2 and magnetic field

First, we discuss the antiferromagnetism of the single orbital 2D model. The local term in Eq. 1 adopts the form

$$H_i = Un_{i\uparrow}n_{i\downarrow} + h(n_{i\uparrow} - n_{i\downarrow}). \quad (6)$$

At  $U=1$  the model is close to the maximal transition temperature between the weak-coupling RPA and strong-coupling Heisenberg regimes [44, 54, 55]. In Fig. 1 we show the evolution of the electron spectral density and the dynamical spin susceptibility across the AFM transition along with the local 1P spectral densities. The location of the studied temperatures in the phase diagram is shown in Fig. 2a. The direction of the staggered magnetization,  $\langle \mathbf{S}_{\mathbf{R}} \rangle = (-1)^{|\mathbf{R}|} \mathbf{N}$  is chosen along the  $x$ -axis. The elements  $\chi^{yy}$  and  $\chi^{zz}$  reflect the two linear Goldstone modes [56] arising from breaking of  $SU(2)$  symmetry in an antiferromagnet. Note, that their spectral weight diverges at the ordering wave vector ( $M$ -point). While the Hamiltonian (1) for  $h = 0$  is isotropic in spin space, the

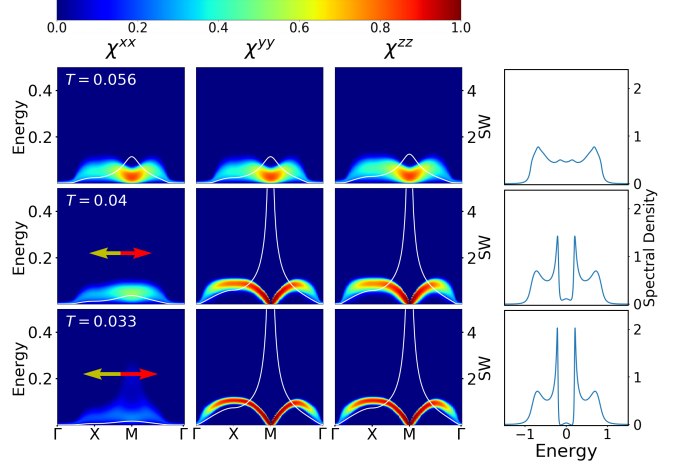


Figure 1. The AFM ordering in the single-band Hubbard model. Left: Imaginary part of the dynamical susceptibility  $\chi(\mathbf{q},\omega)$  ( $\tilde{B}_{\mathbf{k}}(\omega)$  with  $C = 5.5$  is plotted) along the  $\Gamma(0,0)$ – $X(\pi,\pi)$ – $M(2\pi,0)$  path in the extended Brillouin zone for the 2-site unit cell plotted as color plot for various temperatures. The top row corresponds to the normal state at  $T \approx 1.12T_c$ . The lower rows are obtained in the AFM state with  $\mathbf{N}$  along the  $x$ -axis. The white line (right axis) shows the integrated spectral weight  $\Omega_{\mathbf{k}}$ . Right: The corresponding 1P spectral functions.

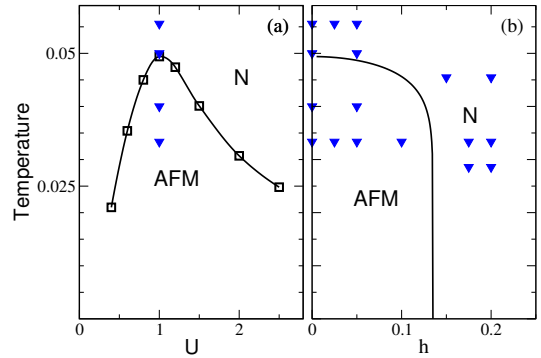


Figure 2. (a) The phase boundary between AFM and normal (N) phase adapted from Ref. 44. (b) The schematic phase diagram in the  $T-h$  plane ( $U = 1$ ). Symbols mark the points of actual calculations.

numerical treatment of  $\chi^{yy}$  is kept independent of that of  $\chi^{zz}$ . Nevertheless, the results reflect the symmetry quite accurately.

Application of a uniform magnetic field is known to polarize an isotropic antiferromagnet perpendicularly to the field,  $\mathbf{N} \perp \mathbf{h}$ , while the spin density acquires a uniform component parallel to the field:  $\langle \mathbf{S}_{\mathbf{R}} \rangle = \mathbf{M} + (-1)^{|\mathbf{R}|} \mathbf{N}$ , with  $\mathbf{M} \parallel \mathbf{h}$ . The symmetry of the Hamiltonian is reduced from  $SU(2)$  to  $U(1)$  [57]. Its breaking leads to a single linear Goldstone mode ( $\chi^{yy}$ ) with polarization

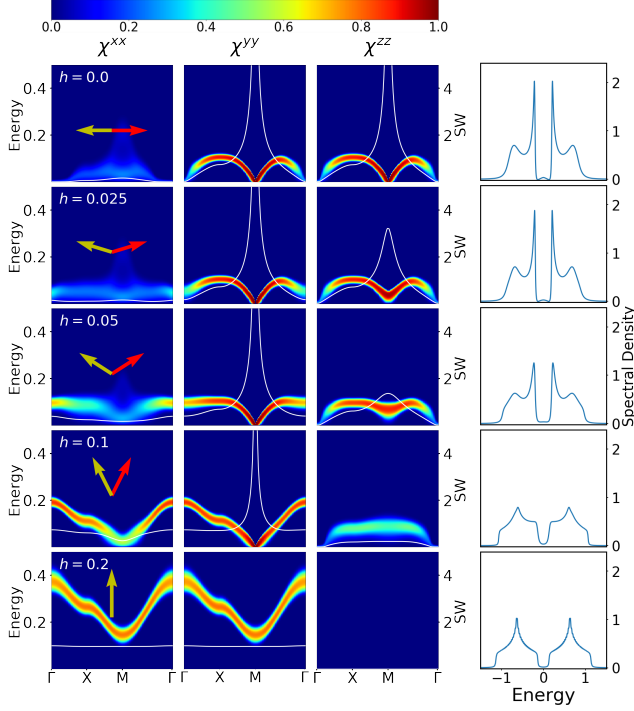


Figure 3. The same as in Fig. 1 for various amplitudes of the external field  $\mathbf{h}$  (along the  $z$ -axis) at  $T = 1/30$ . The top row corresponds to the AFM state without field, the bottom row to a fully polarized normal state. The arrows show the size and tilt of the sublattice spin polarization. The Néel vector  $\mathbf{N}$  points along the  $x$ -axis.

perpendicular to both  $\mathbf{N}$  and  $\mathbf{M}$ , which corresponds to spin rotation in the  $xy$ -plane. Indeed, the  $(\chi^{zz})$  mode polarized along the field direction is gapped, as shown in Fig. 3. At the same time its spectral weight at the  $M$ -point becomes finite.  $\chi^{yy}$  acquires a finite spectral weight at the  $\Gamma$ -point at energy equal to  $2h$  [20]. With increasing  $h$  and progressing tilt of the local moments,  $\chi^{zz}$  loses its spectral weight while the weight of  $\chi^{xx}$  grows from the  $\Gamma$ -point outwards. These observations agree with zero temperature exact diagonalization of Ref. 36, although multimagnon satellites are as expected absent in the DMFT spectra. Eventually, the AFM order is lost, as shown in Fig. 2b, the system becomes fully spin-polarized and recovers the  $U(1)$  symmetry of its Hamiltonian. The perpendicular susceptibilities ( $\chi^{xx}$  and  $\chi^{yy}$ ) describe gapped magnons (perhaps better called magnetic excitons - a spin flip propagating in a spin-polarized background). The field-driven transition can be viewed as the Bose-Einstein condensation of these magnons, which takes place when the magnon gap is closed. The direction of  $\mathbf{N}$  within the  $xy$ -plane plays the role of the condensate phase.

The uniform susceptibilities (at the  $\Gamma$ -point) reflect the

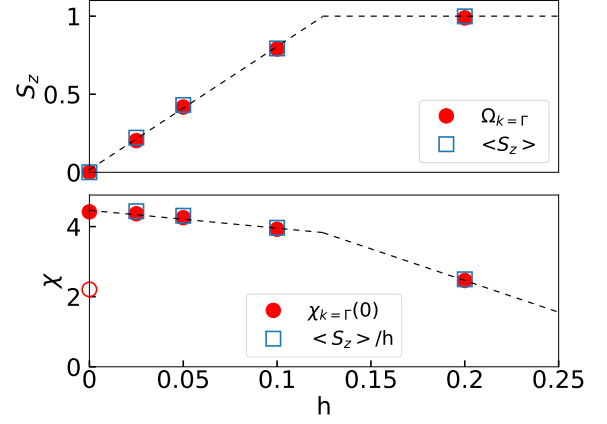


Figure 4. (top) The spectral weight of the transverse ( $xx$  or  $yy$ ) magnons of Fig. 3 compared to the induced moment  $\langle S_z \rangle$ . (bottom) The static uniform transverse susceptibility  $\chi^{xx}(0,0) = \chi^{yy}(0,0)$  compared to its exact value  $\frac{\langle S_z \rangle}{h}$ . The dotted line in the top panel is piecewise: a quadratic fit to the data and a constant (reflecting the spin saturation). In the lower panel the same curve is divided by  $h$ . Note that at  $h = 0$  the equivalence of  $\chi^{xx}$  and  $\chi^{yy}$  is broken. The empty circle marks the value of  $\chi^{xx}(0,0)$ , while the full circle that of  $\chi^{yy}(0,0)$ .

conservation of the total spin moment along the field direction ( $S^z$ ), which leads to (i)  $\chi^{zz}(0, \omega) = \beta \langle (S^z)^2 \rangle \delta(\omega)$  having no dynamics and therefore vanishing imaginary part, (ii)  $\chi^{xx}(0, \omega) = \chi^{yy}(0, \omega)$ . For a simple proof see the Appendix A. Our empirical observations showed that the numerical noise in  $\chi^{\alpha\alpha}(\mathbf{q}, \omega_n)$  is essentially independent of  $\mathbf{q}$ . This is consistent with the fact that such noise mostly originates from the QMC calculation of the local 2PCF, which is used in the determination of the local irreducible vertex. As a consequence, one may subtract  $\chi^{\alpha\alpha}(\mathbf{q}, \omega_n) - \chi^{\alpha\alpha}(0, \omega_n)$  for  $\omega_n > 0$  in order to reduce the noise in cases where (i) holds.

The uniform susceptibility in external field offers further simple consistency tests. First, its static part is exactly  $\chi^{xx}(0,0) = \frac{\langle S_z \rangle}{h}$ , reflecting the fact that application of an infinitesimal transverse field simply rotates the net moment in the new field direction. Second, the spectral weight is equal to the net moment  $\Omega_0^{xx} = \langle S_z \rangle$  (see Eq. D.4 of Ref. 20). Fig. 4 shows that our numerical results respect these properties with great accuracy across all field values.

## B. $S=1$ and single-ion anisotropy

Next, we investigate the effect of single-ion anisotropy on the magnon dispersion. To this end we study a two-

orbital model (at half filling  $n = 2$ )

$$H_i = U \sum_{l=1,2} n_{i l \uparrow} n_{i l \downarrow} + U' \sum_{\sigma, \sigma'} n_{i 1 \sigma} n_{i 2 \sigma'} - J \sum_{\sigma} \left( n_{i 1 \sigma} n_{i 2 \sigma} + \gamma c_{i 1 \sigma}^\dagger c_{i 1 \bar{\sigma}} c_{i 2 \bar{\sigma}}^\dagger c_{i 2 \sigma} \right) \quad (7)$$

with  $U = 1$ ,  $J = 0.25$  and  $U' = 0.5$  [58]. The single ion anisotropy is introduced by unequal weights of the Ising and spin-flip terms in the interaction Hamiltonian. This way the  $SU(2)$  symmetry ( $\gamma = 1$ ) is reduced to a  $Z_2 \times U(1)$  for  $\gamma \neq 1$ . The residual symmetry of the AFM state depends on  $\gamma$ . For  $\gamma > 1$  the atomic ground state corresponds to  $|S, S_z\rangle = |1, 0\rangle$ , i.e., a state with no spin dipole moment. However, for moderate deviations  $\gamma \gtrsim 1$  the inter-site exchange, which favors (dipole) magnetic order, enforces AFM order within the  $xy$ -plane. The in-plane order breaks the  $U(1)$  symmetry and thus one linear Goldstone mode is expected. For  $\gamma < 1$  the atomic ground state corresponds to  $|S, S_z\rangle = |1, \pm 1\rangle$ , i.e., an Ising ground state. The inter-site exchange leads to the formation of AFM order with moments along the  $z$ -axis. The residual symmetry of the ordered state is  $U(1)$  and only the discrete  $Z_2$  symmetry is broken at the transition. Therefore no gapless Goldstone mode is expected. The numerical results are presented in Fig. 5. In the  $SU(2)$  symmetric case we have numerically tested the stability of the AFM state with arbitrary orientation of the Néel vector  $\mathbf{N}$ . We observe two linear Goldstone modes in the response to a field perpendicular to the Néel vector, i.e.,  $\chi^{yy}$  and  $\chi^{zz}$  for  $\mathbf{N} \parallel x$ . For  $\gamma \neq 1$  the system self-consistently picks the expected Néel vector. For  $\gamma > 1$  with the in-plane order, we choose  $\mathbf{N} \parallel x$ . As in the  $SU(2)$  symmetric case we find minor longitudinal response and progressive gapping of the out-of-plane  $\chi^{zz}$  component with increasing  $\gamma$ . For  $\gamma < 1$  the system picks  $\mathbf{N} \parallel z$ . In this case, the residual  $U(1)$  symmetry is reflected in the equivalence of  $\chi^{xx} = \chi^{yy}$ , both of which are progressively gapped when lowering  $\gamma < 1$ .

The presence of a spin gap is known to stabilize the long-range order in 2D. On the other hand, linear gapless magnon mode is detrimental to the long-range order at any finite temperature [17] if the thermal population of this mode is properly taken into account. This is not the case of the DMFT treatment, in which the low-energy long-range spin fluctuations do not feed back to the calculation of the 1P and 2P vertices. Nevertheless, the present results show that DMFT accurately captures the behavior of the spin gap. Therefore it provides a useful reference and a starting point for more sophisticated approaches such as DGA [59, 60] or dual fermions [41, 61]. The model with tunable  $\gamma$  not only hosts both states with gapped and gapless magnons, but allows a continuous tuning between them. Investigation of  $T_c(\gamma)$  dependence may thus provide a useful test of the above methods as well as a quantitative measure of their accuracy.

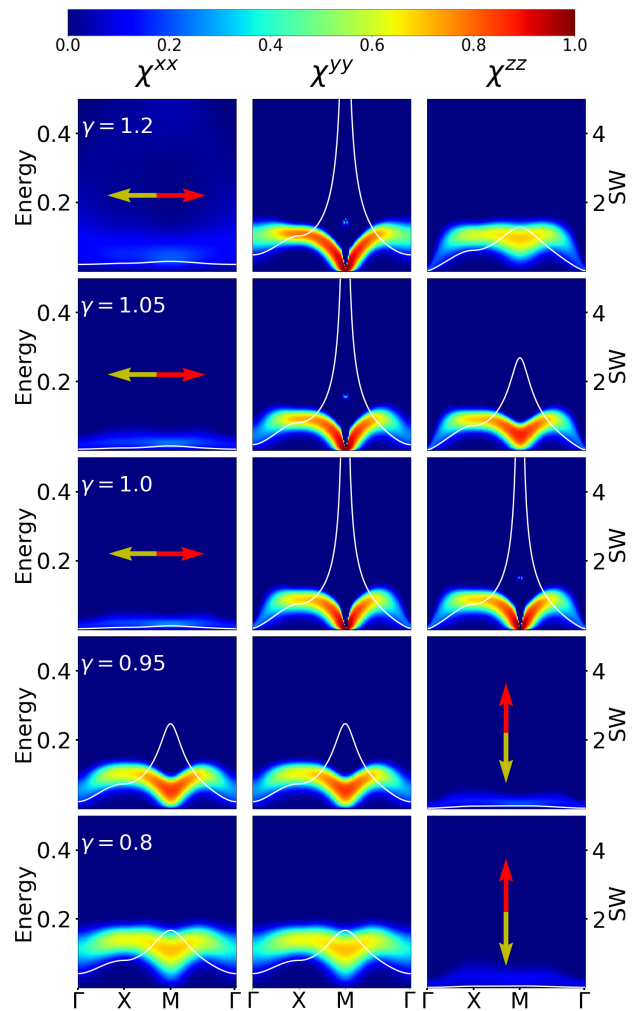


Figure 5. Imaginary part of the dynamical susceptibility  $\chi(\mathbf{q}, \omega)$  ( $\tilde{B}_{\mathbf{k}}(\omega)$  with  $C = 8.5$  is plotted) at  $T = 1/30$  in the AFM state of two-orbital Hubbard model for various single-ion anisotropy. The rows 1-2 correspond to easy ( $xy$ ) plane, row 3 to  $SU(2)$  symmetry, and rows 4-5 to easy ( $z$ ) axis anisotropy. The white line (right axis) shows the the integrated spectral weight  $\Omega_{\mathbf{k}}$ .

### C. $S=3/2$ and spin-orbit coupling

Finally, we study the more realistic 3D case of a three orbital model on a bcc cubic lattice and introduce spin-orbit coupling as the source of spin anisotropy

$$H_i = \sum_{l, l'} \sum_{\sigma, \sigma'} h_{l\sigma, l'\sigma'}^{\text{soc}} c_{i l \sigma}^\dagger c_{i l' \sigma'} + U \sum_l n_{i l \uparrow} n_{i l \downarrow} + U' \sum_{l > l'} \sum_{\sigma, \sigma'} n_{i l \sigma} n_{i l' \sigma'} - J \sum_{l > l'} \sum_{\sigma} \left( n_{i l \sigma} n_{i l' \sigma} + c_{i l \sigma}^\dagger c_{i l \bar{\sigma}} c_{i l' \bar{\sigma}}^\dagger c_{i l' \sigma} \right), \quad (8)$$

where  $U = 2$ ,  $J = 0.5$  and  $U' = 1$ . The form of  $h_{l\sigma, l'\sigma'}^{\text{soc}}$  is given in Appendix B. We point out that the present

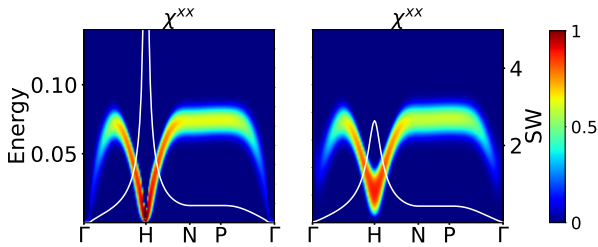


Figure 6. Imaginary part of the transverse dynamical susceptibility  $\chi(\mathbf{q}, \omega)$  ( $\tilde{B}_{\mathbf{k}}(\omega)$  with  $C = 20$  is plotted) at  $T = 1/40$  in the AFM state of 3-orbital Hubbard model ( $\mathbf{N} \parallel z$ -axis) with (right) and without (left) the spin-orbit coupling. The data are plotted along the  $\Gamma(0, 0, 0)$ – $H(2\pi, 0, 0)$ – $N(\pi, \pi, 0)$ – $P(\pi, \pi, \pi)$  path in the extended Brillouin zone for the 2-site unit cell. The white line (right axis) shows the the integrated spectral weight  $\Omega_{\mathbf{k}}$ .

CT-QMC calculation may become impossible at low temperatures due to the sign problem associated with the spin-orbit coupling [62]. Nevertheless, in the half-filled case the effect of spin-orbit coupling is rather moderate [62, 63] and we are able to reach the AFM phase without problems. The Néel vector picks an orientation along a cubic axis ( $\mathbf{N} \parallel z$ ). In Fig. 6 we show the calculated transverse susceptibilities. Without spin-orbit coupling we observe a linear Goldstone mode. The spin-orbit coupling leads to the opening of a finite spin gap. In the 3D case, the AFM order is physically realistic. The DMFT transition temperature  $T_c$  provides a realistic estimate, which misses corrections due to long-range spin fluctuations, while in 2D the corrections dominate.

#### IV. CONCLUSIONS

We have presented DMFT calculations of the AFM phase of the half-filled Hubbard model with one, two and three orbitals in the intermediate coupling regime in two and three dimensions. We find that the expected behavior of magnons in response to external magnetic field or single-ion anisotropy is well captured. While the 3D description of AFM ordering is physically relevant, the ordering behavior in 2D is not correct since DMFT is not sensitive to dimensionality and violates the Mermin-Wagner theorem, which prohibits spontaneous breaking of continuous symmetry at finite temperature. Nevertheless, the fact that DMFT magnons properly describe the opening of the spin gap suggests that DMFT is a good starting point of theories, which properly include the long-range spin fluctuations. The two-orbital model with variable single-ion anisotropy provides an ideal test case for such theories as it allows one to continuously tune between the breaking of a discrete and of a continuous symmetry. On the computational level we have shown that 3-orbital calculations, which cover for example models of ruthenates or iridates, are numerically feasible.

#### ACKNOWLEDGMENTS

The authors thank A. Kauch, F. Krien, J. Kaufmann, A. Toschi and M. Wallerberger for comments and critical reading of the manuscript. This work was supported by the European Research Council (ERC) under the European Union’s Horizon 2020 research and innovation programme (grant agreement No. 646807-EXMAG). D.G was supported by the Czech Science Foundation (GAČR) under Project No. GA19-16937S. The authors acknowledge support by the Czech Ministry of Education, Youth and Sports from the Large Infrastructures for Research, Experimental Development and Innovations project “IT4Innovations National Supercomputing Center – LM2015070”. Part of the calculations were performed at the Vienna Scientific Cluster.

#### Appendix A

The susceptibilities at the  $\Gamma$ -point correspond to correlators of total spin momenta  $S^\alpha = \sum_{\mathbf{R}} S_{\mathbf{R}}^\alpha$ . The Hamiltonian (6) commutes with  $S^z$ ,  $[S^z, H] = 0$ . First, we show that the  $zz$  correlator does not depend on the imaginary time  $\tau$

$$\langle S^z(\tau)S^z \rangle \equiv \langle e^{\tau H} S^z e^{-\tau H} S^z \rangle = \langle (S^z)^2 \rangle.$$

This implies that only  $\chi^{zz}(0, \nu_n = 0)$  is finite and equal to  $\beta \langle (S^z)^2 \rangle$ .

To prove the equality of  $\chi^{xx}$  and  $\chi^{yy}$  we write the corresponding spin-spin correlation functions with the help of ladder operators  $S^x = S^- + S^+$  and  $S^y = i(S^- - S^+)$ :

$$\begin{aligned} \langle S^x(\tau)S^x \rangle &= \langle e^{\tau H} S^+ e^{-\tau H} S^- \rangle + \langle e^{\tau H} S^- e^{-\tau H} S^+ \rangle \\ &\quad + \langle e^{\tau H} S^- e^{-\tau H} S^- \rangle + \langle e^{\tau H} S^+ e^{-\tau H} S^+ \rangle \end{aligned}$$

$$\begin{aligned} \langle S^y(\tau)S^y \rangle &= \langle e^{\tau H} S^+ e^{-\tau H} S^- \rangle + \langle e^{\tau H} S^- e^{-\tau H} S^+ \rangle \\ &\quad - \langle e^{\tau H} S^- e^{-\tau H} S^- \rangle - \langle e^{\tau H} S^+ e^{-\tau H} S^+ \rangle. \end{aligned}$$

Since  $H$  commutes with  $S^z$  only the  $+-$  and  $-+$  contributions are non-zero, while the  $++$  and  $--$  contributions are equal to zero, which implies the  $\Gamma$ -point equality  $\chi^{xx}(0, \omega) = \chi^{yy}(0, \omega)$ .

#### Appendix B

The spin-orbit coupling mimics that in the  $t_{2g}$  subspace of atomic  $d$ -shell [64] commonly found in real materials (with cubic site-symmetry). In the on-site basis  $\{1\uparrow, 1\downarrow, 2\uparrow, 2\downarrow, 3\uparrow, 3\downarrow\}$  it reads

$$h^{\text{SOC}} = -\frac{\zeta}{2} \begin{pmatrix} 0 & 0 & -i & 0 & 0 & 1 \\ 0 & 0 & 0 & i & -1 & 0 \\ i & 0 & 0 & 0 & 0 & -i \\ 0 & -i & 0 & 0 & -i & 0 \\ 0 & -1 & 0 & i & 0 & 0 \\ 1 & 0 & i & 0 & 0 & 0 \end{pmatrix}.$$

- 
- [1] W. Metzner and D. Vollhardt, Phys. Rev. Lett. **62**, 324 (1989).
- [2] A. Georges and G. Kotliar, Phys. Rev. B **45**, 6479 (1992).
- [3] A. Georges, G. Kotliar, W. Krauth, and M. Rozenberg, Rev. Mod. Phys. **68**, 13 (1996).
- [4] G. Kotliar, S. Y. Savrasov, K. Haule, V. S. Oudovenko, O. Parcollet, and C. A. Marianetti, Rev. Mod. Phys. **78**, 865 (2006).
- [5] K. Held, Advances in Physics **56**, 829 (2007).
- [6] M. Jarrell, Phys. Rev. Lett. **69**, 168 (1992).
- [7] L. Boehnke, H. Hafermann, M. Ferrero, F. Lechermann, and O. Parcollet, Phys. Rev. B **84**, 075145 (2011).
- [8] H. Hafermann, E. G. C. P. van Loon, M. I. Katsnelson, A. I. Lichtenstein, and O. Parcollet, Phys. Rev. B **90**, 235105 (2014).
- [9] E. G. C. P. van Loon, H. Hafermann, A. I. Lichtenstein, A. N. Rubtsov, and M. I. Katsnelson, Phys. Rev. Lett. **113**, 246407 (2014).
- [10] E. A. Stepanov, S. Brener, F. Krien, M. Harland, A. I. Lichtenstein, and M. I. Katsnelson, Phys. Rev. Lett. **121**, 037204 (2018).
- [11] H. Park, K. Haule, and G. Kotliar, Phys. Rev. Lett. **107**, 137007 (2011).
- [12] H. Shinaoka, D. Geffroy, M. Wallerberger, J. Otsuki, K. Yoshimi, E. Gull, and J. Kuneš, SciPost Phys. **8**, 012 (2020).
- [13] M. Wallerberger, H. Shinaoka, and A. Kauch, (2020), arXiv:2012.05557.
- [14] J. Otsuki, K. Yoshimi, H. Shinaoka, and Y. Nomura, Phys. Rev. B **99**, 165134 (2019).
- [15] F. Krien, Phys. Rev. B **99**, 235106 (2019).
- [16] A. Katanin, Phys. Rev. B **101**, 035110 (2020).
- [17] N. D. Mermin and H. Wagner, Phys. Rev. Lett. **17**, 1133 (1966).
- [18] E. G. C. P. van Loon, H. Hafermann, A. I. Lichtenstein, and M. I. Katsnelson, Phys. Rev. B **92**, 085106 (2015).
- [19] F. Krien, E. G. C. P. van Loon, H. Hafermann, J. Otsuki, M. I. Katsnelson, and A. I. Lichtenstein, Phys. Rev. B **96**, 075155 (2017).
- [20] F. Krien, *Conserving dynamical mean field approaches to strongly correlated systems*, Ph.D. thesis, University of Hamburg (2018).
- [21] D. Geffroy, J. Kaufmann, A. Hariki, P. Gunacker, A. Hausoel, and J. Kuneš, Phys. Rev. Lett. **122**, 127601 (2019).
- [22] A. Niyazi, D. Geffroy, and J. Kuneš, Phys. Rev. B **102**, 085159 (2020).
- [23] J. Goldston, Nuovo Cim. **19**, 154 (1961).
- [24] Y. Nambu and G. Jona-Lasinio, Phys. Rev. **122**, 345 (1961).
- [25] J. Kuneš, Phys. Rev. B **90**, 235140 (2014).
- [26] J. Kuneš and P. Augustinský, Phys. Rev. B **90**, 235112 (2014).
- [27] J. Nasu, T. Watanabe, M. Naka, and S. Ishihara, Phys. Rev. B **93**, 205136 (2016).
- [28] P. W. Anderson, Phys. Rev. **86**, 694 (1952).
- [29] E. Manousakis, Rev. Mod. Phys. **63**, 1 (1991).
- [30] S. Chakravarty, B. I. Halperin, and D. R. Nelson, Phys. Rev. B **39**, 2344 (1989).
- [31] A. W. Sandvik, Phys. Rev. B **56**, 11678 (1997).
- [32] W. Rowe, J. Knolle, I. Eremin, and P. J. Hirschfeld, Phys. Rev. B **86**, 134513 (2012).
- [33] L. Del Re and A. Toschi, (2021), arXiv:2011.04080.
- [34] Y. M. Vilk, L. Chen, and A.-M. S. Tremblay, Phys. Rev. B **49**, 13267 (1994).
- [35] N. E. Bickers, D. J. Scalapino, and S. R. White, Phys. Rev. Lett. **62**, 961 (1989).
- [36] A. Lüscher and A. M. Läuchli, Phys. Rev. B **79**, 195102 (2009).
- [37] C. N. Varney, C.-R. Lee, Z. J. Bai, S. Chiesa, M. Jarrell, and R. T. Scalettar, Phys. Rev. B **80**, 075116 (2009).
- [38] P. R. C. Kent, M. Jarrell, T. A. Maier, and T. Pruschke, Phys. Rev. B **72**, 060411 (2005).
- [39] S. Fuchs, E. Gull, L. Pollet, E. Burovski, E. Kozik, T. Pruschke, and M. Troyer, Phys. Rev. Lett. **106**, 030401 (2011).
- [40] D. Hirschmeier, H. Hafermann, E. Gull, A. I. Lichtenstein, and A. E. Antipov, Phys. Rev. B **92**, 144409 (2015).
- [41] G. Rohringer, H. Hafermann, A. Toschi, A. A. Katanin, A. E. Antipov, M. I. Katsnelson, A. I. Lichtenstein, A. N. Rubtsov, and K. Held, Rev. Mod. Phys. **90**, 025003 (2018).
- [42] G. Rohringer, A. Toschi, A. Katanin, and K. Held, Phys. Rev. Lett. **107**, 256402 (2011).
- [43] M. Ulmke, V. Janiš, and D. Vollhardt, Phys. Rev. B **51**, 10411 (1995).
- [44] J. Kuneš, Phys. Rev. B **83**, 085102 (2011).
- [45] B. Bauer, L. D. Carr, H. G. Evertz, A. Feiguin, J. Freire, S. Fuchs, L. Gamper, J. Gukelberger, E. Gull, S. Guertler, A. Hehn, R. Igarashi, S. V. Isakov, D. Koop, P. N. Ma, P. Mates, H. Matsuo, O. Parcollet, G. Pawłowski, J. D. Picon, L. Pollet, E. Santos, V. W. Scarola, U. Schollwöck, C. Silva, B. Surer, S. Todo, S. Trebst, M. Troyer, M. L. Wall, P. Werner, and S. Wesel, J. Stat. Mech. Theory Exp. **2011**, P05001 (2011).
- [46] H. Shinaoka, E. Gull, and P. Werner, Comput. Phys. Commun. **215**, 128 (2017).
- [47] A. Gaenko, A. E. Antipov, G. Carcassi, T. Chen, X. Chen, Q. Dong, L. Gamper, J. Gukelberger, R. Igarashi, S. Isakov, M. Könz, J. P. LeBlanc, R. Levy, P. N. Ma, J. E. Paki, H. Shinaoka, S. Todo, M. Troyer, and E. Gull, Comput. Phys. Commun. **213**, 235 (2017).
- [48] P. Werner, A. Comanac, L. de' Medici, M. Troyer, and A. J. Millis, Phys. Rev. Lett. **97**, 076405 (2006).
- [49] J. E. Gubernatis, M. Jarrell, R. N. Silver, and D. S. Sivia, Phys. Rev. B **44**, 6011 (1991).
- [50] J. Kaufmann and K. Held, (2021), arXiv:2105.11211.
- [51] In case of summation over the reciprocal lattice vectors this amounts to  $\frac{1}{N} \sum_{\mathbf{k}}$ , in case of summation over Matsubara frequencies to  $T \sum_{\nu}$ , where  $T$  is the temperature.
- [52]  $F_{\nu} = 1$  in the Matsubara frequency basis.
- [53] J. Otsuki, M. Ohzeki, H. Shinaoka, and K. Yoshimi, Phys. Rev. E **95**, 061302 (2017).

- [54] G. Rohringer and A. Toschi, Phys. Rev. B **94**, 125144 (2016).
- [55] T. Schäfer, N. Wentzell, F. Šimkovic, Y.-Y. He, C. Hille, M. Klett, C. J. Eckhardt, B. Arzhang, V. Harkov, F.-M. Le Régent, A. Kirsch, Y. Wang, A. J. Kim, E. Kozik, E. A. Stepanov, A. Kauch, S. Andergassen, P. Hansmann, D. Rohe, Y. M. Vilc, J. P. F. LeBlanc, S. Zhang, A.-M. S. Tremblay, M. Ferrero, O. Parcollet, and A. Georges, Phys. Rev. X **11**, 011058 (2021).
- [56] H. Watanabe and H. Murayama, Phys. Rev. Lett. **108**, 251602 (2012).
- [57] We mention only the spin symmetries, which are broken or varied in our models and ignore the ones, which are not changed such the global  $U(1)$  due to charge conservation.
- [58] For the sake of simplicity we have omitted the pair-hopping term  $c_{i1\uparrow}^\dagger c_{i1\downarrow}^\dagger c_{i2\downarrow} c_{i2\uparrow} + H.c.$  This term does not affect the broken spin symmetry and is expected to play a minor role when the local high-spin state dominates as in the AFM phases studied here.
- [59] A. Toschi, A. A. Katanin, and K. Held, Phys. Rev. B **75**, 045118 (2007).
- [60] J. Kaufmann, C. Eckhardt, M. Pickem, M. Kitatani, A. Kauch, and K. Held, Phys. Rev. B **103**, 035120 (2021).
- [61] A. N. Rubtsov, M. I. Katsnelson, and A. I. Lichtenstein, Phys. Rev. B **77**, 033101 (2008).
- [62] A. J. Kim, P. Werner, and R. Valentí, Phys. Rev. B **101**, 045108 (2020).
- [63] K.-H. Ahn, K. Pajskr, K.-W. Lee, and J. Kuneš, Phys. Rev. B **95**, 064416 (2017).
- [64] L. Du, L. Huang, and X. Dai, The European Physical Journal B **86** (2013).